Global Sensitivity Analysis for Patient-Specific Aortic Simulations: The Role of Geometry, Boundary Condition and Large Eddy Simulation Modeling Parameters

Huijuan Xu[1]
School of Mechanical Engineering,
Georgia Institute of Technology,
Atlanta, GA 30332;
Siemens Coporate Technology,
Princeton, NJ 08540
e-mails: huijuan.xu@gatech.edu;
huijuan.xu@siemens.com

Davide Baroli
Aachen Institute for Advanced Study in
Computational Engineering Science,
Aachen 52062, Germany
e-mail: baroli@aices.rwth-aachen.de

Alessandro Veneziani
Department of Mathematics,
Emory University,
Atlanta, GA 30322;
Department of Computer Science,
Emory University,
Atlanta, GA 30322
e-mail: ale@mathcs.emory.edu

Numerical simulations for computational hemodynamics in clinical settings require a combination of many ingredients, mathematical models, solvers and patient-specific data. The sensitivity of the solutions to these factors may be critical, particularly when we have a partial or noisy knowledge of data. Uncertainty quantification is crucial to assess the reliability of the results. We present here an extensive sensitivity analysis in aortic flow simulations, to quantify the dependence of clinically relevant quantities to the patient-specific geometry and the inflow boundary conditions. Geometry and inflow conditions are generally believed to have a major impact on numerical simulations. We resort to a global sensitivity analysis, (i.e., not restricted to a linearization around a working point), based on polynomial chaos expansion (PCE) and the associated Sobol' indices. We regard the geometry and the inflow conditions as the realization of a parametric stochastic process. To construct a physically consistent stochastic process for the geometry, we use a set of longitudinal-in-time *images of a patient with an abdominal aortic aneurysm (AAA) to parametrize geometrical variations. Aortic flow is highly disturbed during systole. This leads to high computational costs, even amplified in a sensitivity analysis - when many simulations are needed. To mitigate this, we consider here a large Eddy simulation (LES) model. Our model depends in particular on a user-defined parameter called* filter radius. *We borrowed the tools of the global sensitivity analysis to assess the sensitivity of the solution to this parameter too. The targeted quantities of interest (QoI) include: the total kinetic energy (TKE), the time-average wall shear stress (TAWSS), and the oscillatory shear index (OSI). The results show that these indexes are mostly sensitive to the geometry. Also, we find that the sensitivity may be different during different instants of the heartbeat and in different regions of the domain of interest. This analysis helps to assess the reliability of in silico tools for clinical applications.* [DOI: 10.1115/1.4048336]

1 Introduction

As the computational hemodynamics are progressively incorporated into the clinical practice, a rigorous assessment of the reliability of the numerical predictions is crucial. The numerical solution depends on many factors, ranging from the patient-specific geometry reconstructed from medical images to the measurements used as boundary conditions, the parameters of the mathematical model, and of the associated numerical solver. We do not have a perfect knowledge of these factors and a sensitivity analysis intends to assess the dependence of the computational solution and its associated clinical conclusions on the data as well as the empirically chosen numerical parameters of the solver. Uncertainty quantification is an essential instance of sensitivity analysis, focused on the uncertainty of the physical inputs to a mathematical model, to assess the reliability and the robustness of the numerical solutions.

In this work, we present a sensitivity analysis of the computational hemodynamics in the aorta. The aorta is a peculiar site for the shape, the size, and the regime of the flow. Many pathologies are currently investigated using numerical tools (e.g., Refs. [1–5] to mention a few). An accurate sensitivity analysis in this site is of utmost interest for the reliability of numerical tools.

1.1 Methods of Sensitivity Analysis. Sensitivity analysis can be carried out in different ways. A possible approach is an educated sampling of different values of the inputs under scrutiny to obtain a statistical assessment of the sensitivity. This approach is quite general; it requires many samples for the significance of the results. Another approach resorts to the numerical computation of the so-called *sensitivity equations*. This requires the calculation of the differential equations solved by the *sensitivities*, i.e., the (Gateaux) derivatives of the outputs as a function of the inputs. Numerical procedures can solve these equations. This analysis is "local" as the sensitivities are generally computed by Taylor expansion around a working point, i.e., a nominal value of the inputs. Here, we opted for a "global" sensitivity analysis. Global sensitivity analysis quantifies the importance of varying inputs on the outputs of interest by exploring the entire input parameters' domain [6]. Our approach is based on the polynomial chaos expansion (PCE) and the associated Sobol' indices [7–9]. Recent applications of PCE in vascular problems can be found in Refs. [10–15]. With PCE, the inputs are regarded as stochastic processes represented by a polynomial expansion and parametrized by random input variables. The outputs are, consequently,

[1]Corresponding author.

Manuscript received November 26, 2019; final manuscript received August 14, 2020; published online November 12, 2020. Assoc. Editor: John LaDisa.

represented by a corresponding stochastic polynomial expansion. Our analysis computes the coefficients of a truncated PCE; the number of samples of the input space required to accomplish this task is dictated by the quadrature formulas used for computing these coefficients. The need for samples is significantly less than for other strategies.

1.2 Inputs of Interest. There is a common agreement in computational hemodynamics that the inputs having a major impact on the numerical results with clinical relevance are the geometry and the boundary conditions, more than rheological models or fluid-structure interaction: this is the experience of the authors and experts of the field (e.g., T.J.R. Hughes, personal communication, 2016). Geometry and boundary conditions are, therefore, the focus of the present global sensitivity analysis.

A sensitivity analysis for the geometry can be done in different ways, depending on the specific sources of variations under investigation. For instance, if one is interested in the variations induced by the operator's dependence on a reconstruction procedure, a simple approach consists of sampling the reconstruction with different operators and then comparing the results. The number of samples required to have a statistically significant assessment is pretty large. Here, we pursue a novel approach related to the stochastic parametrization. To obtain physically consistent variations of the geometrical domain parametrized by a random variable, we resort to a *longitudinal* dataset of a patient, i.e., snapshots of the patient's geometry at different times. The patient at hand is affected by an Abdominal Aortic Aneurysm (AAA), and the evolution of the disease is available over a time range of 4 years. With appropriate image-processing techniques (*nonrigid registration*), we manage to create a continuous representation of the geometry as a stochastic process. This enables using PCE in a physically realistic way. Also, we argue that, in this way, our analysis spans a broad range of possible variations and uncertainties of the geometry (image noise, operator dependence, reconstruction artifacts, the time evolution of the morphology).

Investigations of the impact of uncertainty of inflow and outflow boundary conditions on the simulation results of blood flows are, e.g., in Refs. [11] and [13–18]. For the physical nature of the problem, with a strong convective field from the proximal to the distal sites, inflow conditions are arguably more impactful than outflow ones. We postulate that an inlet flowrate is prescribed as a stochastic variable, expanded by PCE. We analyze the impact of the variations of the time-waveform on the numerical results and their hemodynamics significance, with a focus on the different instants of the heartbeat when the sensitivity is significant.

Finally, we extend our sensitivity analysis to numerical parameters required by the blood modeling. As aorta is affected by highly disturbed flows, large Eddy simulation (LES) models have been demonstrated to mitigate the high computational costs significantly [2,19]. However, LES models require numerical parameters whose tuning is largely empirical. In particular, in our model analyzed in Ref. [20] and tested in Refs. [2] and [19], the *filter radius* is expected to have a significant impact on the solution. A local preliminary analysis based on the sensitivities equations in idealized geometries confirmed this guess [21]. Here, we borrow the same tools used for physical inputs to assess our simulations' sensitivity to the filter radius.

1.3 Outputs of Interest. We analyze the impact of the (physical and numerical) inputs for both an idealized aortic geometry and a patient-specific setting, on the following outputs: the total kinetic energy (TKE), the time average wall shear stress (TAWSS), and the oscillatory shear index (OSI). These quantities were demonstrated to be associated with the growth of abdominal aortic aneurysms [22–26]. We use the name of quantities of interest (QoI) hereafter to indicate these model outputs generically. In this way, we assess the robustness of our numerical model for aortic hemodynamic applications. The PCE-based Sobol' indices analysis identifies the inputs that affect the most the final results, while the confidence intervals computed for the numerical simulations certify the reliability of the model predictions.

Our results rigorously confirm the quite general experience of the geometry being the most impactful input on the results. Moreover, the analysis allows a fine investigation of different phases of the heartbeats and the region of the aorta more sensitive to the input variations. In particular, we found that some outputs are more sensitive to the inputs in regions of the vessel where other indices are more robust. If confirmed, this result suggests that a combined calculation of several indices may be beneficial in terms of the overall robustness of the computational clinical indications to the input variations.

2 Materials and Methods

2.1 The Numerical Model. Simulating the aortic blood flows is nontrivial due to the relatively large Reynolds numbers during systole and complex morphology [2,27–29]. The direct numerical simulation of these flows requires a refinement level of the space reticulation to be able to capture the flow field at the smallest significant scale. The associated computational cost might be intimidatingly high, especially for time-sensitive clinical applications. Turbulence modeling has been adopted for simulating aortic flows [28,29]. Recently, an LES deconvolution-based Leray model was shown to capture the properties of a disturbed flow using a relatively coarse discretization finite element mesh, reducing the computational cost [2]. This model can also suppress backflow instability, which is a typical numerical drawback caused by Neumann boundary conditions at outflow branches [19].

The Leray model relies on a modification of the incompressible Navier–Stokes equations. Denoting by $\mathbf{u}$, p the velocity and pressure fields, respectively, in the physical domain Ω and in the time interval $(0,T)$, the Navier–Stokes equations read

$$\rho\frac{\partial \mathbf{u}}{\partial t}+\rho(\mathbf{u}\cdot\nabla)\mathbf{u}-\mu\Delta\mathbf{u}+\nabla p=\mathbf{f} \tag{1}$$

$$\nabla\cdot\mathbf{u}=0 \tag{2}$$

where the first equation states the momentum conservation and the second one the mass conservation. Here, μ denotes the blood viscosity and ρ its density, both assumed constant. The equations are completed by boundary and initial conditions

$$\mathbf{u}=\mathbf{u}_D \quad \text{on} \quad \Gamma_D\times(0,T) \tag{3}$$

$$(\mu\nabla\mathbf{u}-p\mathbf{I})\mathbf{n}=\mathbf{g} \quad \text{on} \quad \Gamma_N\times(0,T) \tag{4}$$

$$\mathbf{u}(t=0)=\mathbf{u}_0 \quad \text{in} \quad \Omega \tag{5}$$

Here, for the sake of the notation, the boundary of Ω is split into two nonoverlapping portions Γ_D (Dirichlet conditions) and Γ_N (Neumann conditions).

In highly disturbed or turbulent flows, the nonlinear term in Eq. (1) determines an energy cascade from large to small scales. This cascade triggers significant effects at space scales smaller than the one of the space discretization of a numerical solver. Eventually, the unresolved scales may trigger numerical instability. For this reason, LES models modify (1) to include the effect of the small space-scales unresolved by the discretization to the ones solved by the numerical problem. In more detail, we introduce an auxiliary velocity field $\mathbf{u}_f$ and solve the following system:

$$\rho\frac{\partial \mathbf{u}}{\partial t}+\rho(\mathbf{u}_f\cdot\nabla)\mathbf{u}-\mu\Delta\mathbf{u}+\nabla p=\mathbf{f} \tag{6}$$

$$\nabla\cdot\mathbf{u}=0 \tag{7}$$

$$-\delta^2\nabla\cdot(a(\mathbf{u})\nabla\mathbf{u}_f)+\mathbf{u}_f+\nabla p_f=\mathbf{u} \tag{8}$$

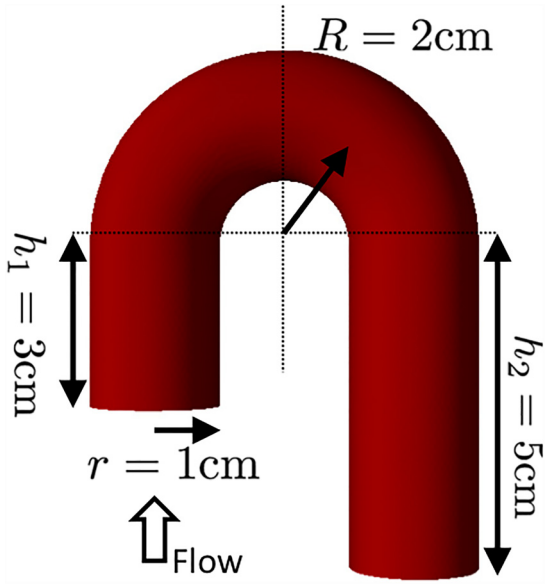

Fig. 1 The simplified aortic arch and its dimensions

$$\nabla \cdot \mathbf{u}_f = 0 \tag{9}$$

with the additional boundary conditions (beyond Eq. (3))

$$\mathbf{u}_f = \mathbf{u}_D \quad \text{on} \quad \Gamma_D \times (0,T) \tag{10}$$

$$(\delta^2 a(\mathbf{u})\nabla \mathbf{u}_f - p_f \mathbf{I})\mathbf{n} = 0 \quad \text{on} \quad \Gamma_N \times (0,T) \tag{11}$$

Here, $a(\mathbf{u})$ is an indicator function that identifies the regions of the fluid domain requiring stabilization, and δ is a user-defined parameter called *filter radius*, which quantifies the strength of the stabilization. For $F \equiv (I - \delta^2\Delta)^{-1}$ (Helmholtz operator), one choice advocated in Refs. [20] and [30] is $a(\mathbf{u}) = |\mathbf{u} - (F(\mathbf{u}))|$ (*deconvolution based indicator function*). In this study we refer to the so-called Evolve-Filter-Relax implementation of this model, as detailed in Ref. [20]. The radius δ should be selected to find the tradeoff between the stabilization (preferring a large δ) and the accuracy (suggesting a small δ).

In what follows, we refer to the solver previously developed in Ref. [2], where the equations are discretized with the finite element method in space (Taylor-Hood elements) and a backward difference formula of order 2 in time with a semi-implicit (Picard) linearization. The solver is implemented in the C++ Object Oriented library lifeV [31]. We carried out simulations on Stampede2 from the extreme science and engineering discovery environment (XSEDE). For all the simulations conducted in the study, we assume blood to be a Newtonian incompressible flow with density $\rho = 1.06\,\mathrm{g/cm^3}$ and viscosity $\mu = 0.035\,\mathrm{dyn \cdot s/cm^2}$. The aortic wall is assumed to be rigid. Time-step, grid size (and grid independence) and the number of heartbeats run to have a reasonable periodic flow are illustrated and discussed in Refs. [2] and [19].

2.2 Benchmarks. The study is carried out on (1) an idealized aortic arch and (2) a patient-specific aorta with a degenerated AAA, i.e., with a degradation of the aortic wall.

2.2.1 The Idealized Aortic Arch. As a proof of concept, we first investigate the impact of the filter radius δ and inflow rate $Q(t)$ in a simplified aortic arch (Fig. 1). The geometry is composed of a half torus and two cylinders. The detailed dimensions are in Fig. 1. In this case, we do not test the uncertainty for the geometry. The stochasticity of the inflow and the filter radius is detailed below.

Fig. 2 Initial (left: acquired at 2010) and follow-up (right: acquired at 2016) aortic geometries of a patient with the AAA

2.2.2 The Patient-Specific Abdominal Aortic Aneurysm. To parametrize realistic variations of the arterial geometry, we considered a patient affected by the AAA, available from the iCardioCloud Project supported by the Cariplo Foundation, Italy (No. 2013–1779). The patient had a significant abdominal aortic dilation from 2010 to 2016, as shown in Fig. 2. The figure reports the 3D reconstruction of the morphology from the available CT scans, performed with the vascular modeling ToolKit [32]. These geometries provided the basis for the construction of the stochastic map needed by the PCE, as explained in Sec. 2.3.1.

2.3 Stochastic Representation of the Inputs. To use the PCE, we associate a stochastic process to the inputs of interest. This avoids the need for many samples, requiring many data currently unavailable. To this aim, we postulate some a priori stochastic information on the inputs. The criterion for these arbitrary choices is the consistency with the physical context.

We list the specific stochastic features of the random variable for each input in Table 1.

2.3.1 Stochastic Representation of the Aneurysmal Geometry. The parametrization of the geometrical variation as a stochastic process can be obtained in different ways. An important criterion is that this task is realistically accomplished. Actually, arbitrary

Table 1 Stochastic inputs and their distributions. Here, $\mathcal{N}(\boldsymbol{\mu}, \boldsymbol{\sigma^2})$ denotes the normal distribution with the mean of μ and variance of σ^2, while $\mathcal{U}[\boldsymbol{a}, \boldsymbol{b}]$ denotes the uniform distribution with the support being $[\boldsymbol{a}, \boldsymbol{b}]$

Uncertain inputs	Distribution	Polynomial chaos
ξ_δ	$\mathcal{N}(h_{\min}, (0.25h_{\min})^2)$	Hermite
ξ_Q	$\mathcal{N}(1, 0.1^2)$	Hermite
ξ_G	$\mathcal{U}[0,1]$	Legendre

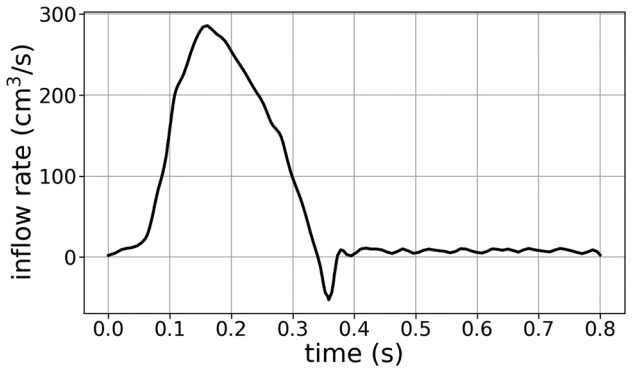

Fig. 3 The mean inflow rate

modifications of a given geometry may lead to unrealistic morphologies. To this aim, we propose here to use the snapshots in different time instances available for our AAA patient. Once the reconstructions of the geometries have been obtained at the different stages of the pathology (Fig. 2), we consider these as the realizations of a stochastic process function of a random variable ξ_G, uniformly distributed between 0 and 1 (in short $\xi_G \sim \mathcal{U}[0,1]$). In detail, the 2010 geometry corresponds to $\xi_G = 0$ and the follow-up (2016) to $\xi_G = 1$. The three-dimensional deformation field $D(\mathbf{x})$ quantifying the variation between the initial (Fig. 2 left) and follow-up (Fig. 2 right) geometries is computed by a nonrigid registration method [33], as already successfully carried out in a previous study [2] to quantify the growth of an aortic dissection. Once the deformation map $D(\mathbf{x})$ is computed, it is scaled by ξ_G to represent the uncertainty in the morphology. The resulting uncertain geometry is a linear function of the parameter ξ_G

$$G(\mathbf{x}, \xi_G) = G_{\text{initial}}(\mathbf{x}) + \xi_G \times D(\mathbf{x}) \tag{12}$$

To the best of our knowledge, it is the first time that a sensitivity analysis on geometry is conducted by using a longitudinal dataset and a registration method. In this way we embrace a large range of possible realizations of the geometry, on a time scale of 4 years. The same procedure can be used on different time scales and with more than two scans, adjusting the scaling function (12) accordingly.

2.3.2 Stochastic Representation of the Inflow Rate. In the absence of patient-specific inflow data, we designed a stochastic inflow $Q(t) = q(t)\xi_Q$ by scaling the average inflow waveform $q(t)$ reported in Fig. 3 (retrieved from Ref. [34]) by a normally distributed univariate random variable $\xi_Q \sim \mathcal{N}(\mu_Q, \sigma_Q^2)$, where $\mu_Q = 1$ and $\sigma_Q = 0.1$. This results in a range $(\mu_Q \pm 3\sigma_Q)$ of peak inflow being from 203 to 380 ml/s, covering the flowrate from at rest to stress [35].

2.3.3 Stochastic Representation of the Filter Radius δ. The filter radius δ is modeled as a normally distributed univariate random variable $\xi_\delta \sim \mathcal{N}(\mu_\delta, \sigma_\delta^2)$ with mean being the minimal mesh size $\mu_\delta = h_{\min}$ and standard deviation being $\sigma_\delta = 25\%\mu_\delta$. As we mentioned in the introduction, this parameter is empirically tuned as a tradeoff between stabilization (preferring a larger value) and accuracy (suggesting a smaller value). The standard deviation 25% of the "nominal" value is a reasonable range in our practical experience.

2.4 Model Responses (Outputs). The model responses considered here are the TKE, TAWSS, and OSI. These are indices with potential relevance for clinical applications in aortic diseases (see, e.g., Refs. [34] and [36–38]).

The TKE is defined as

$$\text{TKE} \equiv \frac{1}{2}\int_\Omega \rho \mathbf{u} \cdot \mathbf{u} d\Omega$$

where Ω represents the whole computational domain.

The wall shear stress (WSS) is defined as the tangential component of the normal stress. The normal stress for a Newtonian fluid is defined as

$$\mathbf{w} = p\mathbf{n} - \mu(\nabla \mathbf{u} + \nabla^{\mathrm{T}}\mathbf{u}) \cdot \mathbf{n}$$

and correspondingly the WSS reads

$$\text{WSS} \equiv \mathbf{w} - (\mathbf{w} \cdot \mathbf{n})\mathbf{n}$$

The TAWSS is defined as the time average over the heart beat of duration T of the WSS

$$\text{TAWSS} = \frac{1}{T}\int_0^T \text{WSS}(t) dt$$

The OSI [39] is a way for measuring the occurrence of retrograde flows during the heart beat on the wall and it is defined as

$$\text{OSI} = \frac{1}{2}\left(1 - T\frac{|\text{TAWSS}|}{\int_0^T |\text{WSS}|(t) dt}\right)$$

OSI of values around $(1/2)$ indicates a high occurrence of retrograde flows.

The mean and variance of these QoIs are computed as well as the corresponding Sobol' indices to quantify the relative contribution of different uncertain inputs to the uncertainty of QoIs.

2.5 Recall on Global Sensitivity Analysis. We recall the basic ingredients of our global sensitivity analysis, the Sobol' index, and their determination through PCE. The notation in this section follows the previous literature [8,40,41].

2.5.1 The Sobol' Index. The Sobol' index is a variance-based indicator to characterize the dependence of the output variance on the stochastic inputs [42], so to rank the influence of the inputs, especially for nonlinear models [7,8,40]. Sobol proved that the output of a model can be decomposed into summands with increasing dimensions of the input parameters [42]. Let $\boldsymbol{\xi} = (\xi_1, \ldots, \xi_d)$ represent the vector of d inputs, which are independent random variables with a joint distribution $\pi(\boldsymbol{\xi})$ defined on the sample space Ω of a probability measure space $(\Omega, \mathcal{F}, P)$, where P is the probability measure defined on the sigma-algebra $\mathcal{F}$. The Sobol' decomposition [43] of the model output, generically denoted by f, reads

$$\begin{aligned} f(\boldsymbol{\xi}) &= f_0 + \sum_{i=1}^{d} f_i(\xi_i) + \sum_{i_1,i_2 \in \mathcal{C}(2,d)} f_{i_1 i_2}(\xi_{i_1}, \xi_{i_2}) \\ &\quad + \sum_{i_1,i_2,i_3 \in \mathcal{C}(3,d)} f_{i_1 i_2 i_3}(\xi_{i_1}, \xi_{i_2}, \xi_{i_3}) + \cdots f_{1,\ldots,d}(\xi_1, \ldots, \xi_d) \\ &= \sum_{s=0}^{d} \sum_{i_1,\ldots,i_s \in \mathcal{C}(s,d)} f_{i_1,\ldots,i_s}(\xi_{i_1}, \ldots \xi_{i_s}) \end{aligned} \tag{13}$$

where f_0 is a constant and $\mathcal{C}(s,d)$ denotes all the possible combinations of s elements of the pool of indices $1, 2, \ldots, d$.

With a little abuse of notation, we introduce the index sets $A = \{i_1, \ldots, i_s\} \subset \{1, \ldots, d\}$ for $s = 1, \ldots, d$, so that the decomposition (13) for $\boldsymbol{\xi}_A = (\xi_{i_1}, \ldots, \xi_{i_s})$ can be written as

$$f(\boldsymbol{\xi}) = \sum_{A \subset \{1,\ldots,d\}} f_A(\boldsymbol{\xi}_A) \tag{14}$$

with the convention that for $A = \emptyset$, then $f_A := f_0$. By the construction of the decomposition, the summands satisfy

$$\int f_A(\boldsymbol{\xi}_A)\pi(\xi_i) d\xi_i = 0, \quad \forall i \in A \tag{15}$$

The orthogonality between the summands follows as:

$$\int f_A(\xi_A) f_B(\xi_B)\pi(\xi)d\xi \tag{16}$$

$$= \delta_{AB}\int f_A(\xi_A) f_A(\xi_A)\pi(\xi)d\xi \tag{17}$$

$\forall A, B \subset \{1,\ldots,d\}$, where δ_{AB} is the Kronecker delta ($\delta_{AB} = 1$ for $A \equiv B$; $\delta_{AB} = 0$ otherwise).

Due to the orthogonality, the total and partial expectations of the output are

$$\mathbb{E}(f) = \int f(\xi)\pi(\xi)d\xi = f_0 \tag{18}$$

$$\mathbb{E}(f_A) = \int f_A(\xi_A)\pi(\xi_A)d\xi_A = 0 \tag{19}$$

The total variance and partial variances are defined as

$$V := \mathrm{Var}[f] = \mathbb{E}(f^2 - \mathbb{E}(f)^2) = \int f(\xi)^2\pi(\xi)d\xi - f_0^2 \tag{20}$$

$$V_A := \mathrm{Var}[f_A] = \mathbb{E}(f_A^2 - \mathbb{E}(f_A)^2) = \int f_A^2(\xi_A)\pi(\xi_A)d\xi_A \tag{21}$$

Subsequently, the Sobol' indices [43] corresponding the specific set A of inputs are defined as the ratios between the partial variances and the total variance

$$S_A = V_A/V \tag{22}$$

which are the global sensitivity indices indicating the functional structure of the model [43] related to the combination of the input parameters ξ_A. Notice that $f_A = 0$ if and only if $V_A = 0$.

2.5.2 Polynomial Chaos Expansion Based Sobol' Indices. Traditionally, the Sobol' indices are computed using Monte Carlo (MC) or other sampling methods [42]. To be accurate, MC approaches generally require many samples, since the accuracy improves with only the square root of the number of samples. In our case, each sample requires the numerical simulation of the LES model, with a prohibitive computational cost. Therefore, we resort to the truncated PCE for a surrogate model to propagate uncertainties and compute the Sobol' indices. In this way, the computational cost reduces to that of estimating the coefficients of the PCE. Specifically, the convergence of the Sobol's indices from PCE depends on: (1) the smoothness of the output of interest, (2) the number of dimensions of the inputs under consideration [8,44]. To balance the computational cost and accuracy, we test here truncated PCE of degree 2 and 3 (see Sec. 3).

2.5.3 Truncated Polynomial Chaos Expansion. Any second-order random process (i.e., with a finite variance) can be represented as a series of polynomials in random inputs [45,46]. Denote again by $\xi \equiv \{\xi_i\}_{i=1}^{\infty}$ a vector of independent random variables with a joint distribution $\pi(\xi)$ defined on $(\Omega, \mathcal{F}, P)$. The corresponding image probability space of the random variables is $(\Gamma, \mathcal{B}(\Gamma), \pi(\xi)d\xi)$, where Γ is the image of ξ, $\mathcal{B}(\Gamma)$ is the Borel σ-algebra on Γ and $\pi(\xi)d\xi$ is the probability measure defined on $\mathcal{B}(\Gamma)$. Consider

$\mathbb{P}_p$ as the space of all polynomials in ξ_i with degree up to p;

$\hat{\mathrm{P}}_p$ as the set of all polynomials in $\mathbb{P}_p$ orthogonal to $\mathbb{P}_{p-1}$ with respect to the probability measure $\pi(\xi)d\xi$;

$\bar{\mathbb{P}}_p$ as the space of polynomials spanned by $\hat{\mathrm{P}}_p$.

The subspace $\bar{\mathbb{P}}_p$ is called the pth homogeneous Chaos [47] originally and $\hat{\mathrm{P}}_p$ is called the polynomial chaos of order p. For $(t, \mathbf{x}) \in [0, T] \times \mathcal{D}$, a random process $u(t, \mathbf{x}, \xi)$ can be represented as

$$\begin{aligned} u(t,\mathbf{x},\xi) = u_0(t,\mathbf{x})\hat{\mathrm{P}}_0 + \sum_{i_1=1}^{\infty} u_{i_1}(t,\mathbf{x})\hat{\mathrm{P}}_1(\xi_{i_1}) \\ + \sum_{i_1=1}^{\infty}\sum_{i_2=1}^{i_1} u_{i_1 i_2}(t,\mathbf{x})\hat{\mathrm{P}}_2(\xi_{i_1},\xi_{i_2}) \\ + \sum_{i_1=1}^{\infty}\sum_{i_2=1}^{i_1}\sum_{i_3=1}^{i_2} u_{i_1 i_2 i_3}(t,\mathbf{x})\hat{\mathrm{P}}_3(\xi_{i_1},\xi_{i_2},\xi_{i_3}) + \cdots \end{aligned} \tag{23}$$

with $u_{i_1 i_2 \ldots}(t, \mathbf{x})$ being the deterministic coefficients. This expansion can be rewritten as

$$u(t,\mathbf{x},\xi) = \sum_{k=0}^{\infty} u_k(t,\mathbf{x})\Phi_k(\xi) \tag{24}$$

There is a one to one correspondence between the functionals $\hat{\mathrm{P}}_p$ and Φ_k. Therefore Φ_k are orthogonal polynomial basis with respect to probability measure, i.e.,

$$\begin{aligned} \int \Phi_i(\xi)\Phi_j(\xi)\pi(\xi)d\xi \\ = \delta_{ij}\int \Phi_i(\xi)\Phi_i(\xi)\pi(\xi)d\xi \\ = \delta_{ij}||\Phi_i(\xi)||^2 \end{aligned} \tag{25}$$

Φ_0 is conventionally taken as $\Phi_0 = 1$. Due to the orthogonality, $\mathbb{E}(\Phi_i) = 0$ for all $i > 0$.

In practice, only a finite set of d input parameters are considered with polynomial basis of limited degrees no greater than p. The truncated polynomial chaos expansion reads

$$u(t,\mathbf{x},\xi) = \sum_{k=0}^{K} u_k(t,\mathbf{x})\Phi_k(\xi) \tag{26}$$

where $K + 1 = (p + d)!/p!d!$.

The multivariate polynomial basis with degree up to p can be constructed by the tensor product of unidimensional basis

$$\Phi_k(\xi) = \Phi_{\boldsymbol{\alpha}^k}(\xi) := \prod_{i=1}^{n}\phi_{\alpha_i^k}(\xi_i) \tag{27}$$

where $\boldsymbol{\alpha}^k = (\alpha_1^k, \ldots, \alpha_d^k) \in \mathbb{N}^n$ with $|\boldsymbol{\alpha}^k| = \sum_{i=1}^n \alpha_i^k \le p$, $n \le d$ and $k = 0, 1, \ldots K$. The moments of the output random process can be computed based on the PCE with minimum computational effort. For a fixed $(t, \mathbf{x})$, the mean and variance of $u(t, \mathbf{x}, \xi)$ is given by

$$\mathbb{E}[u(t,\mathbf{x},\xi)] \simeq u_0(t,\mathbf{x}) \tag{28}$$

$$\mathrm{Var}[u(t,\mathbf{x},\xi)] \simeq \sum_{k=1}^{K} u_k(t,\mathbf{x})^2||\Phi_k||^2 \tag{29}$$

2.5.4 Polynomial Chaos Expansion-Based Sobol' Indices. The summands of the Sobol's decomposition, depending only on the subset of ξ indicated by the index set A, can be approximated using PCE as

$$f_A(t,\mathbf{x},\xi) \simeq f_A^{PC}(t,\mathbf{x},\xi) \tag{30}$$

In order to regroup the multidimensional polynomial basis $\Phi_{\boldsymbol{\alpha}}$ that depends only on a subset of parameters $A = \{i_1, \ldots, i_s\} \subset \{1, \ldots, d\}$ with $|A| := \mathrm{card}(A)$, define the sets

$$I_A := \{k \in \{1,\ldots,K\} : \Phi_k = \prod_{i=1}^{|A|} \phi_{\alpha_i^k}(\xi_{A_i}), \boldsymbol{\alpha}^k \in \mathbb{N}^d, |\boldsymbol{\alpha}^k| \le p\}.$$

Therefore we have

$$f_A^{PC}(t,\mathbf{x},\xi_A) := \sum_{k\in I_A} f_k(t,\mathbf{x})\Phi_k(\xi_A) \tag{31}$$

where $f_k(t,\mathbf{x})$ is the deterministic coefficient.

Consequently, we approximate the Sobol' decomposition by the truncated polynomial expansion as

$$\begin{aligned} f^{\mathrm{PC}}(t,\mathbf{x},\xi) &\simeq \sum_{A\subset\{1,\ldots,d\}} f_A^{\mathrm{PC}}(t,\mathbf{x},\xi_A) \\ &= \sum_{k\in I_A} f_k(t,\mathbf{x})\Phi_k(\xi_A) \end{aligned} \tag{32}$$

Due to the orthogonality of the polynomial basis, the total variance and partial variance can be conveniently computed as

$$V^{PC} := \mathrm{Var}[f^{\mathrm{PC}}] = \sum_{k=1}^{K} y_k(t,\mathbf{x})^2 ||\Phi_k||^2 \tag{33}$$

$$V_A^{PC} := \mathrm{Var}[f_A^{\mathrm{PC}}] = \sum_{k\in I_A} y_k(t,\mathbf{x})^2 ||\Phi_k||^2. \tag{34}$$

Then, the PCE based Sobol' indices read

$$S_A^{\mathrm{PC}} = V_A^{\mathrm{PC}}/V^{\mathrm{PC}} \tag{35}$$

Specifically, first-order Sobol indices quantify the contribution of the total variance from the sole input parameter ξ_i

$$S_i^{\mathrm{PC}} = \frac{\sum_{k\in I_{A_i}} f_k(t,\mathbf{x})^2 ||\Phi_k||^2}{\sum_{k=1}^{K} f_k(t,\mathbf{x})^2 ||\Phi_k||^2} \tag{36}$$

where $A_i = \{i\}$ for $i = 1,\ldots,d$. As shown in Eq. (36), the cost of computing the Sobol' indices corresponds to the cost of evaluating the coefficients of the truncated PCE.

2.6 Computing the Coefficients of the Polynomial Expansion. There are different approaches to accomplishing this task. "Intrusive approaches" (i.e., Galerkin approach [40,48]) and "nonintrusive" (point collocation [49] and pseudo-spectral projection) methods [49–51] are used to compute the stochastic modes for the PCE. In the former, the governing equations are reformulated to target the PCE. In the latter, available deterministic solvers are combined with collocation or projection techniques. *Compressed sensing* is usually adopted with the point collocation method to enforce the sparsity of the coefficients [9].

The computational complexity of the fluid-dynamics application at hand and the dimension of the input parameter space are significant. We opted for the nonintrusive pseudo-spectral method due to its relatively low computational cost. This basically means that, like for any generalized Fourier series, the coefficients are computed by numerical integration (quadrature). By taking advantage of the orthogonality, the deterministic coefficients can be approximated by the quadrature formula

$$f_k(t,\mathbf{x}) = \frac{\int f(t,\mathbf{x},\xi)\Phi_k \pi(\xi) d\xi}{\int \Phi_k^2 \pi(\xi) d\xi} \tag{37}$$

$$\simeq \frac{1}{||\Phi_k||^2} \sum_{r=1}^{R} f(t,\mathbf{x},\xi^r)\Phi_k(\xi^r)\pi(\xi^r)w^r \tag{38}$$

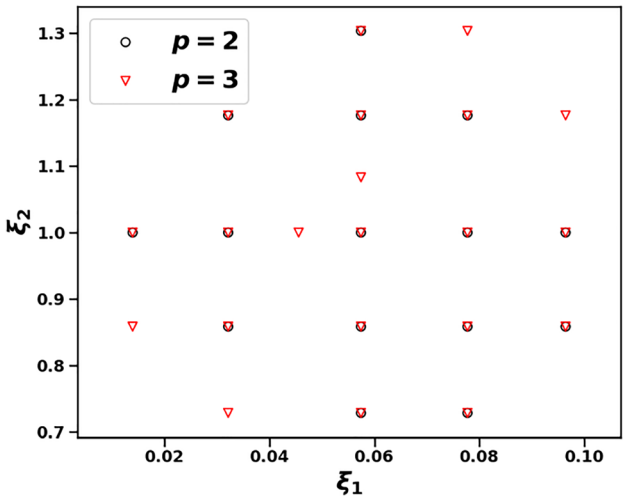

Fig. 4 The Leja sparse quadrature points for PCE of degree two and three with the two-dimensional input parameter space

where ξ^r and w^r are quadrature points and associated weights. The number of required numerical simulations (ultimately, the computational complexity of the method) and the accuracy depend on the number and the collocation of the quadrature nodes. We adopted nested sparse grid quadrature points based on Leja sequence [52] and generated by the open-source tool Chaospy [53]. In this way, the number of forward simulations required for evaluating the stochastic modes for $d = 2$ and a PCE of degree 2 is 15 while it is 21 for PCE of degree 3, as shown in Fig. 4. Here, the number of quadrature points are subjected to an "empirical rule" as detailed in Ref. [52], which is implemented in Chaospy. This is much less than the number of samples required by MC approaches. Further potential improvement can be made by adopting adaptive sparse PCE [54,55], which is subject to future work. The degree of the surrogate PCE is cross-validated by comparing its results to the results of the original LES model.

3 Results

3.1 Results on the Idealized Aortic Arch. As a proof of concept, the impact of the filter radius $\delta = \xi_\delta$ and inflow rate $Q(t) = q(t)\xi_Q$ are investigated in a simplified aortic arch (Fig. 1). Details of the random input parameters are listed in first two rows of Table 1.

The truncated PCE approximations of the TKE, TAWSS are computed with polynomial basis of degree $p = 2$ and $p = 3$. As anticipated, in this case, $d = 2$, we needed 15 and 21 simulations, respectively. The differences between the results from the PCE of different degrees are negligible.

The mean, variance, and prediction interval of the TKE for the simplified aortic are shown in Fig. 5. The Sobol' indices for the TKE is shown in Fig. 6 (left).

The mean, variance, and prediction interval for TAWSS are reported in Fig. 7, while the Sobol' indices for TAWSS is shown in Fig. 6 (right).

3.2 Results on the Patient-Specific Abdominal Aortic Aneurysm. The truncated PCE approximations of the TKE, TAWSS, and OSI are computed with PCE of degree $p = 2$. We compute the stochastic modes using the nonintrusive pseudo-spectral methods with the Leja nested sparse grid quadrature points. The resulting number of simulations required is 35 ($d = 3$ inputs in this case). To be concrete, the realizations of the geometry in the five different values of ξ_G are illustrated in Fig. 8.

The mean and coefficient of variation for the TAWSS (top row) and OSI (bottom row) are reported in Fig. 9. The Sobol' indices

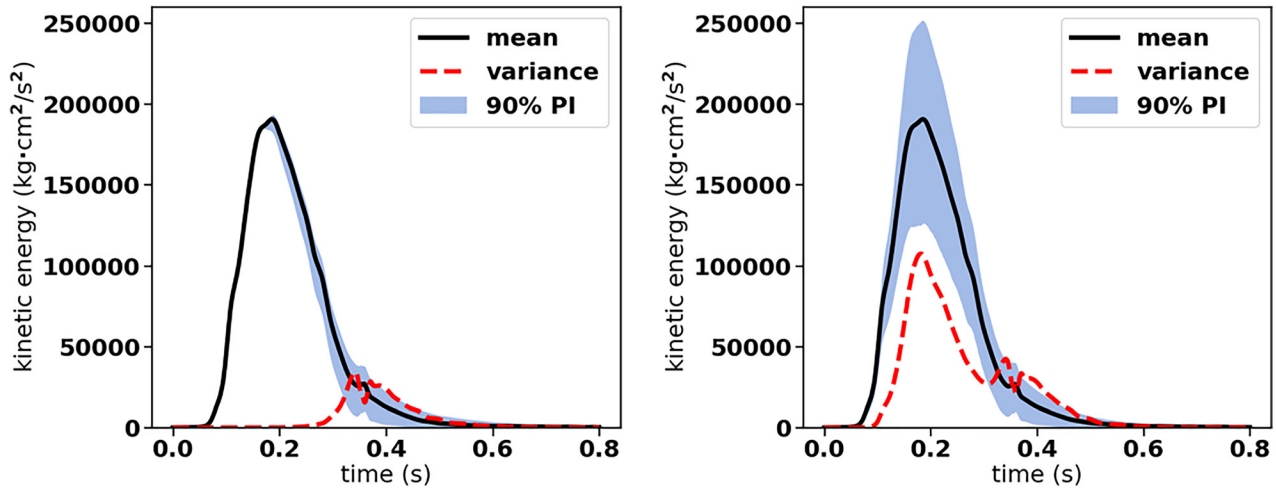

Fig. 5 The mean, variance, 90% prediction interval for the TKE in the simplified aortic arch. Only the uncertainty of the filter radius δ is considered in the left plot; The uncertainty of both the filter radius δ and inflow rate $Q(t)$ are considered in the right plot.

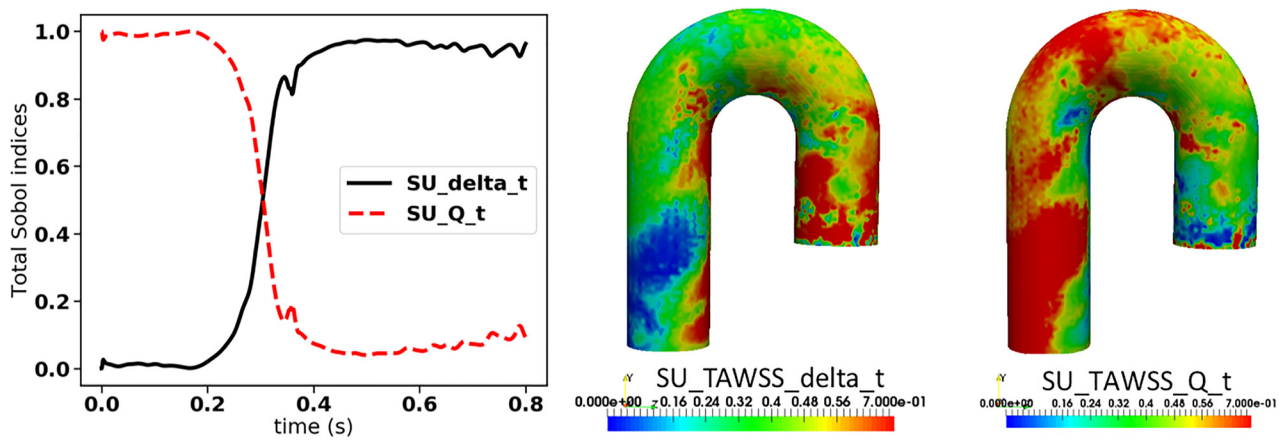

Fig. 6 Sobol' indicies of filter radius and inflow for TKE (left) and TAWSS (right). *SU_delta_t* and *SU_Q_t* denote the total Sobol' index of the filter radius δ and inflow for TKE, respectively. *SU_TAWSS_delta_t* and *SU_TAWSS_Q_t* denote the total Sobol' index of δ for TAWSS and inflow for TAWSS, respectively.

for the TKE, TAWSS, and OSI are reported in Figs. 10 and 11, respectively.

4 Discussion

4.1 The Idealized Case. The variance of the TKE caused by the variation of the filter radius δ during the systole (from 0 to 0.3 s) is minimal, while the influence of the filter radius is evident during the diastole, as shown in Fig. 5 (left). However, the inflow impact is much higher than that caused by δ, as shown in Fig. 5 (right).

4.1.1 Sobol' Indices for the Total Kinetic Energy. The relative influence of the variations of the filter radius δ as well as the inflow boundary conditions on the hemodynamic factors of this simplified aortic arch are investigated using the Sobol' indices. The Sobol' index of δ in time (Fig. 6 left) represents the contribution of δ to the TKE variation through the cardiac cycle. Consistent with the variance results (in Fig. 5), this Sobol' index is much lower than that from the inflow rate during systole, despite the higher coefficient of variation (CoV) of δ. This result demonstrates the robustness of the model during systole. However, the influence of δ exceeds that of the inflow rate during diastole.

The TAWSS Sobol' index of δ is lower than that of the inflow in most of the arch, except for the inflow and the interior bend. The higher Sobol' index of δ in these regions might be due to the influence of the δ during the diastolic phase.

4.2 The Patient-Specific Abdominal Aortic Aneurysm Case. TAWSS and OSI are often computed together to assess the nature of the flow in the neighborhood of the wall, and the connection to possible focal diseases or degenerations of the wall. As expected, the mean TAWSS is found to be lower in the region with more growth than other regions on the aneurysm. Correspondingly, we found that OSI is relatively high in the region with more growth. These two hemodynamics indicators point out a possible disturbed oscillating nature of the flow in the region with growth.

More interestingly, the CoV for TAWSS is higher in the region with more growth (i.e., region with relatively low mean TAWSS), while the opposite result is observed from OSI. This means that

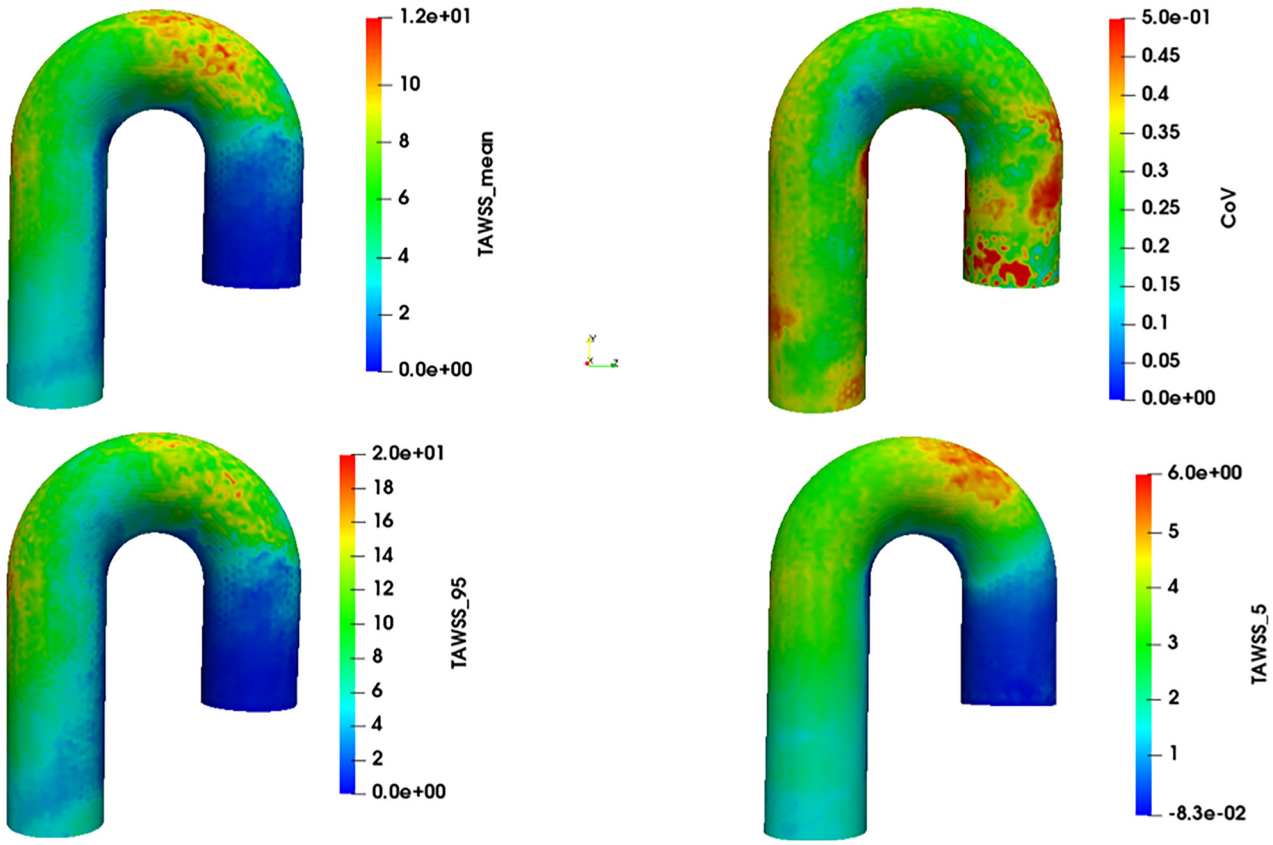

Fig. 7 Mean, coefficient of variation, 95th percentile, 5th percentile of TAWSS of the simplified aortic arch

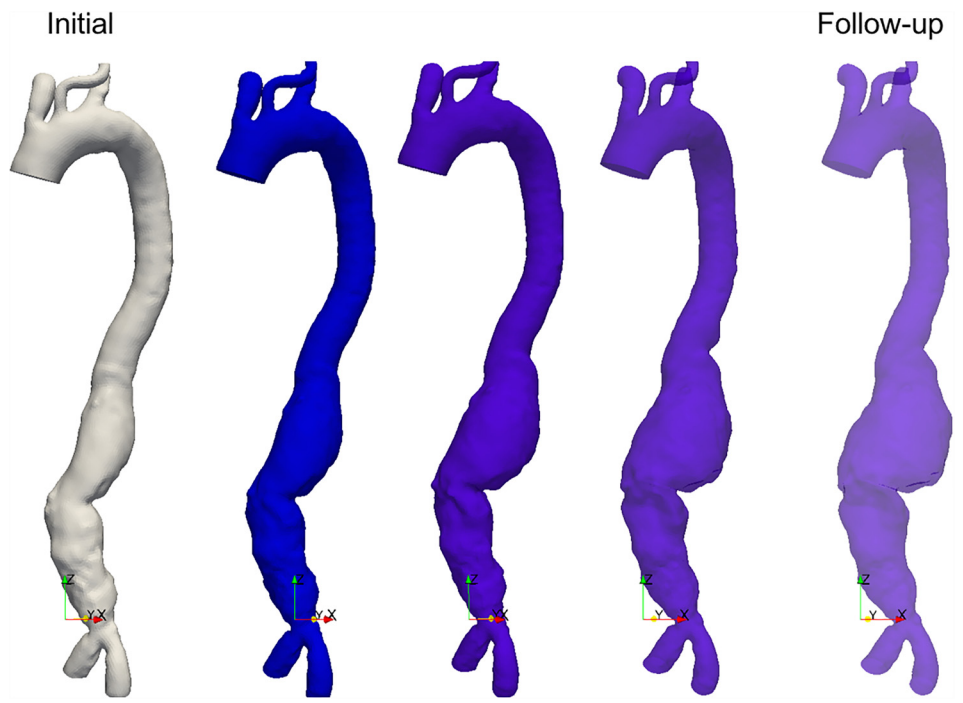

Fig. 8 The sampled AAA geometries corresponding to five values of ξ_G in the quadrature nodes

the reliability of the two hemodynamic indices is somehow complementary in terms of space-dependent reliability. Their joint computation is justified by the fact that one is more reliable where the other is less.

4.2.1 Sobol' Indices for the Total Kinetic Energy. The Sobol' indices of the filter radius δ, the inflow rate, as well as the abdominal aneurysmal geometry for the TKE are in Fig. 10. The result for the relative contribution from the filter radius and inflow rate

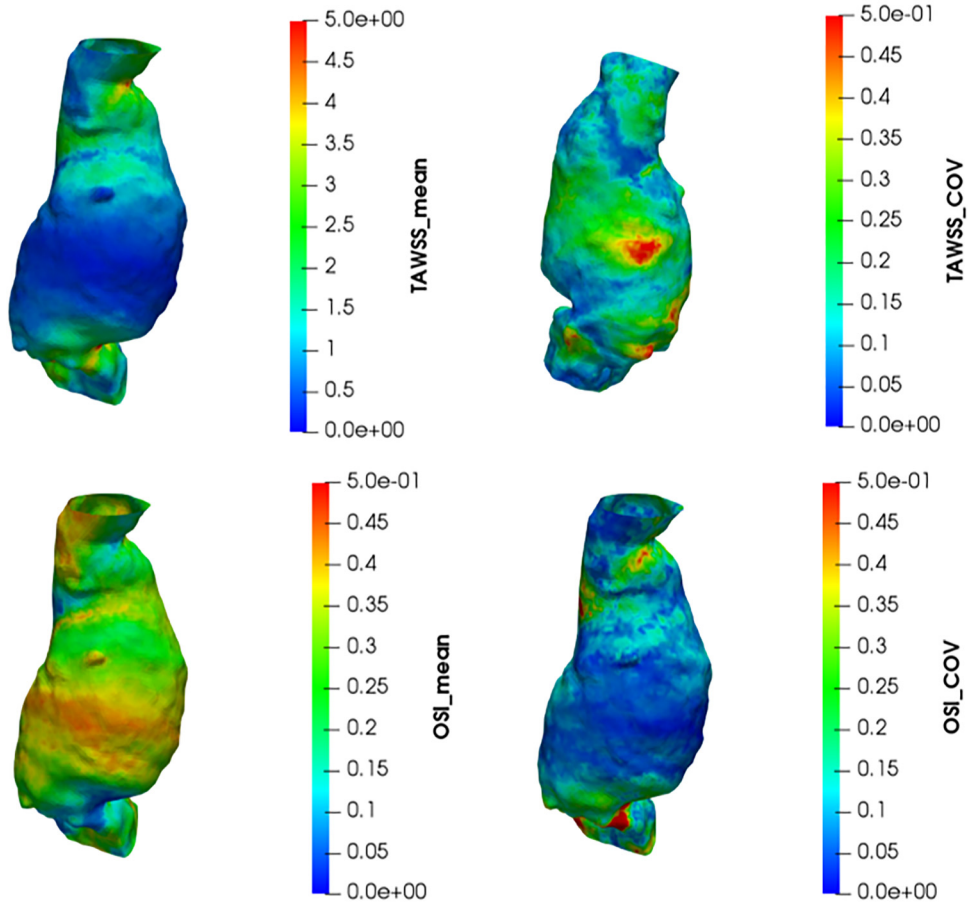

Fig. 9 Mean and coefficient of variation of TAWSS (top) and OSI (bottom) for the patient-specific AAA case

is consistent with the finding from the simplified aortic arch, i.e., the inflow rate has relatively more contribution to the total variation during systole. In contrast, the filter radius is more influential than the inflow rate during diastole. However, the variation of the abdominal aneurysmal geometry of the aorta has a significantly dominant role for the variability of the TKE throughout the whole cardiac cycle. The partial variance caused by the variation in the geometry is larger than those caused by the other two factors combined, as shown in Fig. 10.

4.2.2 Sobol' Indices for the Time-Average Wall Shear Stress and Oscillatory Shear Index. The Sobol' indices of the filter radius δ, inflow rate, as well as the abdominal aneurysmal geometry for TAWSS and OSI are in Fig. 11. Similarly to what we found for the TKE, the relative contribution of the three investigated factors (ranked from high to low) to both TAWSS and OSI are the aneurysm geometry, the inflow rate, and the filter radius. The TAWSS of the two extreme quadrature points for ξ_G is in Fig. 12 and the OSI is in Fig. 13. The filter radius and inflow rate are frozen at their mean values, respectively. We can appreciate that the TAWSS and OSI may change significantly even when the geometry is the only source of variability.

4.3 Limitations. The work bears some limitations, as listed below.

(1) Due to the constraint of computational costs, only three sources of uncertainty are considered simultaneously.
(2) We assume simplified models for the variations in the inflow boundary condition for the lack of patient-specific data of a large population.
(3) In the simulations, the arterial wall is rigid, and the flow is Newtonian.

Limitations (1) and (2) will be addressed in future works, while we speculate that the limitations in (3) have a minor impact on the conclusions of this study. We argue that the qualitative conclusions drawn from the results here, particularly in terms of

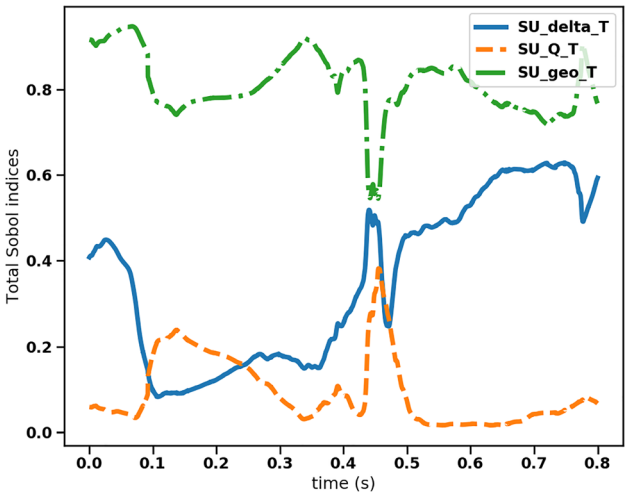

Fig. 10 Sobol' indices for the TKE for the patient-specific AAA case. (*SU_delta_T*, *SU_Q_T* and *SU_geo_T* represent the total Sobol' indices of δ, inflow and geometry, respectively).

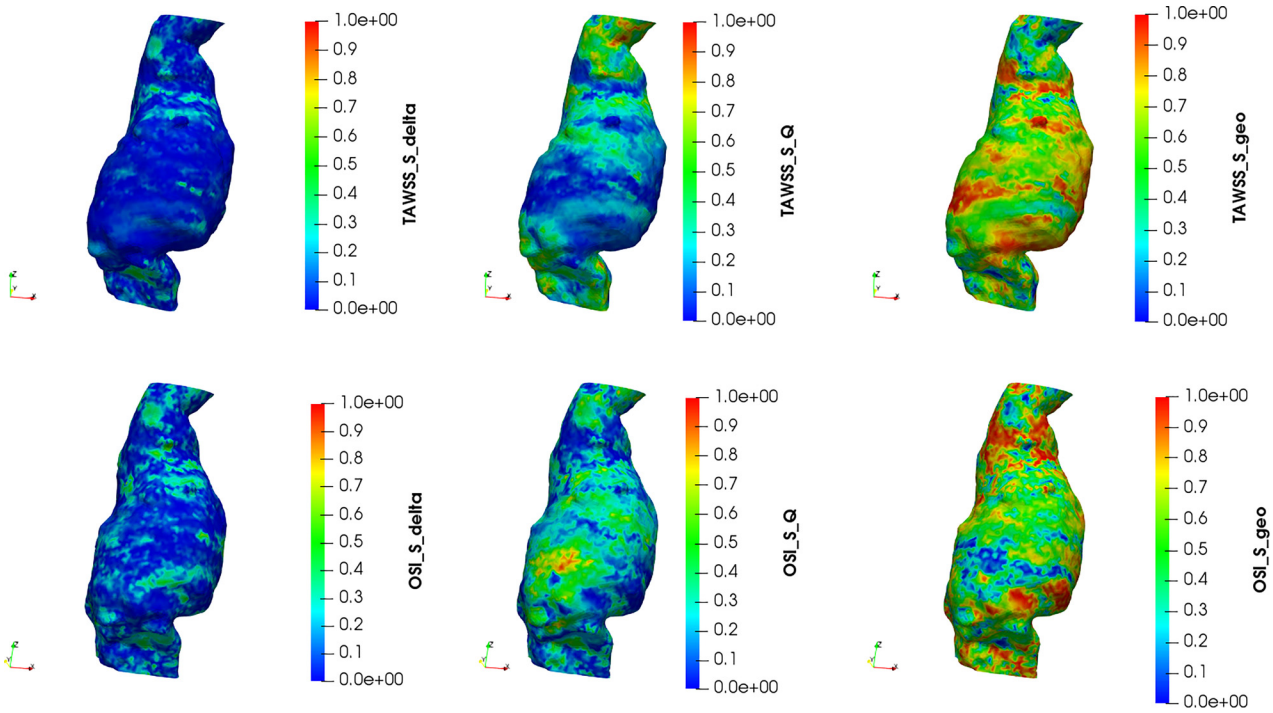

Fig. 11 Sobol' indices for TAWSS (top row) and OSI (bottom row) for the patient-specific AAA case. Notice that the color scale associated with the bars is the same in the three panels.

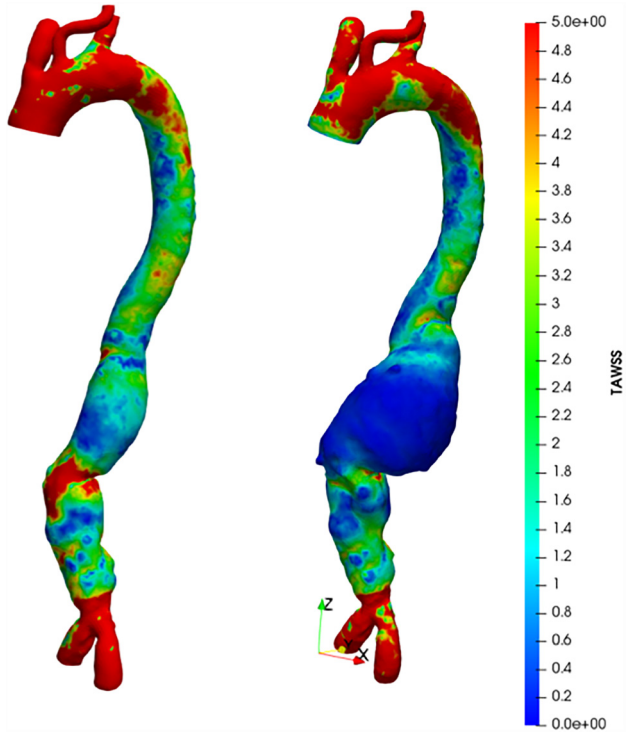

Fig. 12 TAWSS for the extreme geometries $\xi_G = 0$ (left) and $\xi_G = 1$ (right) for the patient-specific AAA case, when $\xi_\delta = \mu_\delta$ and $\xi_G = \mu_G$

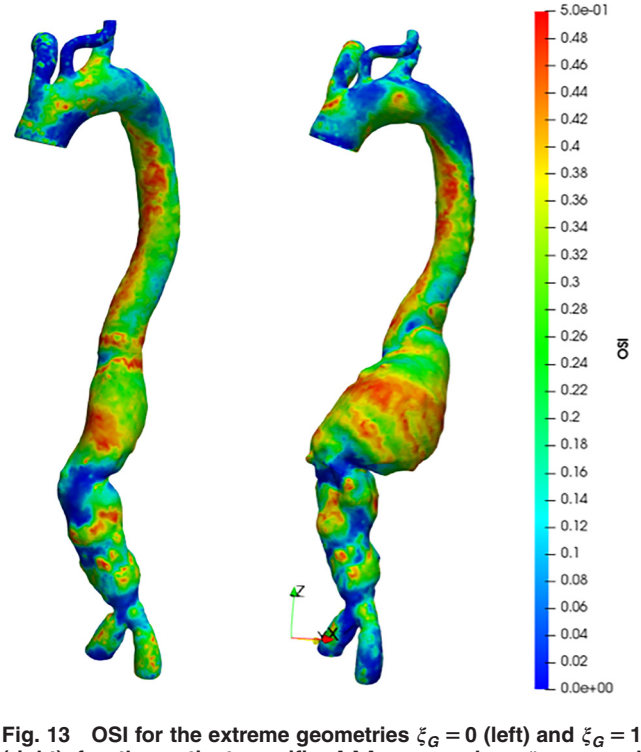

Fig. 13 OSI for the extreme geometries $\xi_G = 0$ (left) and $\xi_G = 1$ (right) for the patient-specific AAA case, when $\xi_\delta = \mu_\delta$ and $\xi_G = \mu_G$

prioritizing the impact of the different uncertainties hold despite these limitations.

5 Conclusions

We performed a global sensitivity analysis using PCE-based Sobol' indices to investigate the impact of the filter radius of the deconvolution-based Leray model, inflow rate, as well as the geometry on the hemodynamic simulations in aortas. The conclusions of the results are summarized hereafter.

(1) Arterial morphology has always been speculated to be a critical factor affecting the computational hemodynamic predictions. The results in this study confirm this intuition:

the geometry is the most influential uncertain input, comparing to the other inputs considered. Other studies report similar results on idealized geometries. In Ref. [12], the authors considered idealized AAA and carotid sinus geometries [12] with the radius of the aneurysm as an uncertain input. Thanks to our novel use of the image-registration procedure, coupled with the truncated PCE analysis, we can extend the results to patient-specific geometries with a realistic geometrical variability. We observed significant variations of wall shear stress and axial velocity fields with the variation of the geometry. For completeness, we mention that in coronary arteries, the relative importance of the minimal luminal diameter was shown to exceed that of the viscosity and boundary resistance in computing FFR_{CT} [15]. Our results lead to a similar conclusion in the aorta. In this respect, *it is crucial to use patient-specific geometries and to quantify the associated sensitivity to predict clinically relevant results reliably*.

(2) Minimal influence of δ on clinically relevant quantities is shown by the Sobol' index of δ for TAWSS and OSI in the patient-specific AAA case, as shown in Fig. 11. *These numerical results demonstrated that the clinical QoIs are quite insensitive to the filter radius and therefore we can guarantee the robustness of applying the Leray model in aortic simulations*.

(3) The third practical conclusion we want to highlight from our results is that *different hemodynamic indices may show a different level of reliability in space*. The CoV results of TAWSS and OSI in the patient-specific AAA case of this study seem to "complement each other," in the sense that one is more trustworthy in a specific region where the other is less reliable and vice versa. This result suggests that it is worth computing both in practice and complementing mutually the information they provide to have a complete, reliable picture of the clinical condition of the patient, so to use one or the other QoIs in different regions of interest.

The educated (possibly automatic) combination of the different QoIs in clinical scenarios and the extension of the present global analysis to more uncertain inputs will be the subject of future works. Specifically, we target the sensitivity analysis on the aortic syndrome of type B aortic dissections in our following work and its impact on the clinical routine of diagnosis of this specific disease.

Acknowledgment

We gratefully acknowledge the help of Romarowski Rodrigo (San Donato Hospital, Milan, IT, and University of Pavia, IT) for the patient-specific CT images.

Funding Data

- We carried out simulations on this study on the Extreme Science and Engineering Discovery Environment (XSEDE), which is supported by the National Science Foundation (Grant No. TG-ASC160069; Funder ID: 10.13039/100000001).
- H. Xu and A. Veneziani acknowledge the support of the U.S. National Science project NSF-DMS 1620406/1620384 "Collaborative Research: Efficient Modeling of Incompressible Fluid Dynamics at Moderate Reynolds Numbers" (Funder ID: 10.13039/100000001).

References

[1] Romarowski, R. M., Lefieux, A., Morganti, S., Veneziani, A., and Auricchio, F., 2018, "Patient-Specific Cfd Modelling in the Thoracic Aorta With Pc-Mri–Based Boundary Conditions: A Least-Square Three-Element Windkessel Approach," Int. J. Numer. Methods Biomed. Eng., **34**(11), p. e3134.

[2] Xu, H., Piccinelli, M., Leshnower, B. G., Lefieux, A., Taylor, W. R., and Veneziani, A., 2018, "Coupled Morphological–Hemodynamic Computational Analysis of Type b Aortic Dissection: A Longitudinal Study," Ann. Biomed. Eng., **46**(7), pp. 927–939.

[3] Gallo, D., Steinman, D. A., Bijari, P. B., and Morbiducci, U., 2012, "Helical Flow in Carotid Bifurcation as Surrogate Marker of Exposure to Disturbed Shear," J. Biomech., **45**(14), pp. 2398–2404.

[4] Xu, X., Borghi, A., Nchimi, A., Leung, J., Gomez, P., Cheng, Z., Defraigne, J.-O., and Sakalihasan, N., 2010, "High Levels of 18f-Fdg Uptake in Aortic Aneurysm Wall Are Associated With High Wall Stress," Eur. J. Vasc. Endovascular Surg., **39**(3), pp. 295–301.

[5] Auricchio, F., Conti, M., Lefieux, A., Morganti, S., Reali, A., Sardanelli, F., Secchi, F., Trimarchi, S., and Veneziani, A., 2014, "Patient-Specific Analysis of Post-Operative Aortic Hemodynamics: A Focus on Thoracic Endovascular Repair (Tevar)," Comput. Mech., **54**(4), pp. 943–953.

[6] Saltelli, A., Ratto, M., Andres, T., Campolongo, F., Cariboni, J., Gatelli, D., Saisana, M., and Tarantola, S., 2008, *Global Sensitivity Analysis: The Primer*, John Wiley & Sons, Hoboken, NJ.

[7] Sudret, B., 2008, "Global Sensitivity Analysis Using Polynomial Chaos Expansions," Reliab. Eng. Syst. Saf., **93**(7), pp. 964–979.

[8] Crestaux, T., Le Maitre, O., and Martinez, J.-M., 2009, "Polynomial Chaos Expansion for Sensitivity Analysis," Reliab. Eng. Syst. Saf., **94**(7), pp. 1161–1172.

[9] Huan, X., Safta, C., Sargsyan, K., Geraci, G., Eldred, M. S., Vane, Z. P., Lacaze, G., Oefelein, J. C., and Najm, H. N., 2018, "Global Sensitivity Analysis and Estimation of Model Error, Toward Uncertainty Quantification in Scramjet Computations," AIAA J., **56**(3), pp. 1170–1184.

[10] Guzzetti, S., Alvarez, L. M., Blanco, P., Carlberg, K., and Veneziani, A., 2020, "Propagating Uncertainties in Large-Scale Hemodynamics Models Via Network Uncertainty Quantification and Reduced-Order Modeling," Comput. Methods Appl. Mech. Eng., **358**, p. 112626.

[11] Tran, J. S., Schiavazzi, D. E., Kahn, A. M., and Marsden, A. L., 2019, "Uncertainty Quantification of Simulated Biomechanical Stimuli in Coronary Artery Bypass Grafts," Comput. Methods Appl. Mech. Eng., **345**, pp. 402–428.

[12] Sankaran, S., and Marsden, A. L., 2011, "A Stochastic Collocation Method for Uncertainty Quantification and Propagation in Cardiovascular Simulations," ASME J. Biomech. Eng., **133**(3), p. 031001.

[13] Boccadifuoco, A., Mariotti, A., Celi, S., Martini, N., and Salvetti, M. V., 2016, "*Uncertainty Quantification in Numerical Simulations of the Flow in Thoracic Aortic Aneurysms*," Institute of Structural Analysis and Antiseismic Research, School of Civil Engineering, National Technical University of Athens, Ntua, Athens, Greece, pp. 6226–6249.

[14] Brault, A., Dumas, L., and Lucor, D., 2017, "Uncertainty Quantification of Inflow Boundary Condition and Proximal Arterial Stiffness–Coupled Effect on Pulse Wave Propagation in a Vascular Network," Int. J. Numer. Methods Biomed. Eng., **33**(10), p. e2859.

[15] Sankaran, S., Kim, H. J., Choi, G., and Taylor, C. A., 2016, "Uncertainty Quantification in Coronary Blood Flow Simulations: Impact of Geometry, Boundary Conditions and Blood Viscosity," J. Biomech., **49**(12), pp. 2540–2547.

[16] Valen-Sendstad, K., Piccinelli, M., KrishnankuttyRema, R., and Steinman, D. A., 2015, "Estimation of Inlet Flow Rates for Image-Based Aneurysm Cfd Models: Where and How to Begin?," Ann. Biomed. Eng., **43**(6), pp. 1422–1431.

[17] Bozzi, S., Morbiducci, U., Gallo, D., Ponzini, R., Rizzo, G., Bignardi, C., and Passoni, G., 2017, "Uncertainty Propagation of Phase Contrast-Mri Derived Inlet Boundary Conditions in Computational Hemodynamics Models of Thoracic Aorta," Comput. Methods Biomech. Biomed. Eng., **20**(10), pp. 1104–1112.

[18] D'Elia, M., and Veneziani, A., 2013, "Uncertainty Quantification for Data Assimilation in a Steady Incompressible Navier-Stokes Problem," ESAIM: Math. Modell. Numer. Anal., **47**(4), pp. 1037–1057.

[19] Xu, H., Baroli, D., Di Massimo, F., Quaini, A., and Veneziani, A., 2020, "Backflow Stabilization by Deconvolution-Based Large Eddy Simulation Modeling," J. Comput. Phys., **404**, p. 109103.

[20] Bertagna, L., Quaini, A., and Veneziani, A., 2016, "Deconvolution-Based Nonlinear Filtering for Incompressible Flows at Moderately Large Reynolds Numbers," Int. J. Numer. Methods Fluids, **81**(8), pp. 463–488.

[21] Bertagna, L., Quaini, A., Rebholz, L. G., and Veneziani, A., 2019, "On the Sensitivity to the Filtering Radius in Leray Models of Incompressible Flow," *Contributions to Partial Differential Equations and Applications*, Springer, Berlin, pp. 111–130.

[22] Salsac, A.-V., Sparks, S., Chomaz, J.-M., and Lasheras, J., 2006, "Evolution of the Wall Shear Stresses During the Progressive Enlargement of Symmetric Abdominal Aortic Aneurysms," J. Fluid Mech., **560**, pp. 19–51.

[23] Les, A. S., Shadden, S. C., Figueroa, C. A., Park, J. M., Tedesco, M. M., Herfkens, R. J., Dalman, R. L., and Taylor, C. A., 2010, "Quantification of Hemodynamics in Abdominal Aortic Aneurysms During Rest and Exercise Using Magnetic Resonance Imaging and Computational Fluid Dynamics," Ann. Biomed. Eng., **38**(4), pp. 1288–1313.

[24] Arzani, A., Suh, G.-Y., Dalman, R. L., and Shadden, S. C., 2014, "A Longitudinal Comparison of Hemodynamics and Intraluminal Thrombus Deposition in Abdominal Aortic Aneurysms," Am. J. Physiol.-Heart Circ. Physiol., **307**(12), pp. H1786–H1795.

[25] Boyd, A. J., Kuhn, D. C., Lozowy, R. J., and Kulbisky, G. P., 2016, "Low Wall Shear Stress Predominates at Sites of Abdominal Aortic Aneurysm Rupture," J. Vasc. Surg., **63**(6), pp. 1613–1619.

[26] Qiu, Y., Yuan, D., Wen, J., Fan, Y., and Zheng, T., 2018, "Numerical Identification of the Rupture Locations in Patient-Specific Abdominal Aortic Aneurysmsusing Hemodynamic Parameters," Comput. Methods Biomech. Biomed. Eng., **21**(1), pp. 1–12.
[27] Formaggia, L., Quarteroni, A., and Veneziani, A., 2010, *Cardiovascular Mathematics: Modeling and Simulation of the Circulatory System*, Vol. 1, Springer Science & Business Media, Berlin.
[28] Lantz, J., Ebbers, T., Engvall, J., and Karlsson, M., 2013, "Numerical and Experimental Assessment of Turbulent Kinetic Energy in an Aortic Coarctation," J. Biomech., **46**(11), pp. 1851–1858.
[29] Ha, H., Ziegler, M., Welander, M., Bjarnegård, N., Carlhäll, C.-J., Lindenberger, M., Länne, T., Ebbers, T., and Dyverfeldt, P., 2018, "Age-Related Vascular Changes Affect Turbulence in Aortic Blood Flow," Front. Physiol., **9**, p. 36.
[30] Layton, W. J., and Rebholz, L. G., 2012, *Approximate Deconvolution Models of Turbulence: Analysis, Phenomenology and Numerical Analysis*, Vol. 2042, Springer Science & Business Media, Berlin.
[31] Bertagna, L., Deparis, S., Formaggia, L., Forti, D., and Veneziani, A., 2017, "The Lifev Library: Engineering Mathematics Beyond the Proof of Concept," arXiv preprint: 1710.06596.
[32] Antiga, L., Piccinelli, M., Botti, L., Ene-Iordache, B., Remuzzi, A., and Steinman, D. A., 2008, "An Image-Based Modeling Framework for Patient-Specific Computational Hemodynamics," Med. Biol. Eng. Comput., **46**(11), pp. 1097–1112.
[33] Myronenko, A., and Song, X., 2010, "Point Set Registration: Coherent Point Drift," IEEE Trans Pattern Anal Mach. Intell., **32**(12), pp. 2262–2275.
[34] Cheng, Z., Tan, F., Riga, C., Bicknell, C., Hamady, M., Gibbs, R., Wood, N., and Xu, X., 2010, "Analysis of Flow Patterns in a Patient-Specific Aortic Dissection Model," ASME J. Biomech. Eng., **132**(5), p. 051007.
[35] Pibarot, P., Blais, C., Dumesnil, J. G., Burwash, I. G., Beanlands, R. S., Mundigler, G., Loho, N., Rader, F., Baumgartner, H., Chayer, B., Kadem, L., Garcia, D., and Durand, L.-G., 2006, "Projected Valve Area at Normal Flow Rate Improves the Assessment of Stenosis Severity in Patients With Low-Flow, Low-Gradient Aortic Stenosis: The Multicenter Topas (Truly or Pseudo-Severe Aortic Stenosis) Study-Response," Circulation, **114**(14), pp. E527–E527.
[36] Boussel, L., Rayz, V., McCulloch, C., Martin, A., Acevedo-Bolton, G., Lawton, M., Higashida, R., Smith, W. S., Young, W. L., and Saloner, D., 2008, "Aneurysm Growth Occurs at Region of Low Wall Shear Stress Patient-Specific Correlation of Hemodynamics and Growth in a Longitudinal Study," Stroke, **39**(11), pp. 2997–3002.
[37] den Reijer, P. M., Sallee, D., van der Velden, P., Zaaijer, E. R., Parks, W. J., Ramamurthy, S., Robbie, T. Q., Donati, G., Lamphier, C., Beekman, R. P., and Brummer, M. E., 2010, "Hemodynamic Predictors of Aortic Dilatation in Bicuspid Aortic Valve by Velocity-Encoded Cardiovascular Magnetic Resonance," J. Cardiovasc. Magn. Reson., **12**(1), p. 4.
[38] Chen, D., Müller-Eschner, M., Kotelis, D., Böckler, D., Ventikos, Y., and von Tengg-Kobligk, H., 2013, "A Longitudinal Study of Type-b Aortic Dissection and Endovascular Repair Scenarios: Computational Analyses," Med. Eng. Amp Phys., **35**(9), pp. 1321–1330.
[39] Ku, D. N., Giddens, D. P., Zarins, C. K., and Glagov, S., 1985, "Pulsatile Flow and Atherosclerosis in the Human Carotid Bifurcation. Positive Correlation Between Plaque Location and Low Oscillating Shear Stress," Aeterioscler. Thromb. Vasc. Biol., **5**(3), pp. 293–302.
[40] Ghanem, R. G., and Spanos, P. D., 2003, *Stochastic Finite Elements: A Spectral Approach*, Courier Corporation, Chelmsford, MA.
[41] Sudret, B., 2007, "Uncertainty Propagation and Sensitivity Analysis in Mechanical Models–Contributions to Structural Reliability and Stochastic Spectral Methods," *Habilitationa Diriger Des Recherches*, Université Blaise Pascal, Clermont-Ferrand, France.
[42] Sobol, I. M., 1993, "Sensitivity Estimates for Nonlinear Mathematical Models," Math. Modell. Comput. Exp., **1**(4), pp. 407–414.
[43] Sobol, I. M., 2001, "Global Sensitivity Indices for Nonlinear Mathematical Models and Their Monte Carlo Estimates," Math. Comput. Simul., **55**(1–3), pp. 271–280.
[44] Najm, H. N., 2009, "Uncertainty Quantification and Polynomial Chaos Techniques in Computational Fluid Dynamics," Annu. Rev. Fluid Mech., **41**(1), pp. 35–52.
[45] Cameron, R. H., and Martin, W. T., 1947, "The Orthogonal Development of Non-Linear Functionals in Series of Fourier-Hermite Functionals," Ann. Math., **48**(2), pp. 385–392.
[46] Xiu, D., and Karniadakis, G. E., 2003, "Modeling Uncertainty in Flow Simulations Via Generalized Polynomial Chaos," J. Comput. Phys., **187**(1), pp. 137–167.
[47] Wiener, N., 1938, "The Homogeneous Chaos," Am. J. Math., **60**(4), pp. 897–936.
[48] Bäck, J., Nobile, F., Tamellini, L., and Tempone, R., 2011, "Stochastic Spectral Galerkin and Collocation Methods for Pdes With Random Coefficients: A Numerical Comparison," *In Spectral and High Order Methods for Partial Differential Equations*, Springer, Springer, Berlin, pp. 43–62.
[49] Hosder, S., Walters, R., and Perez, R., 2006, "A Non-Intrusive Polynomial Chaos Method for Uncertainty Propagation in Cfd Simulations," AIAA Paper No. AIAA 2006-891.
[50] Gottlieb, D., and Orszag, S. A., 1977, *Numerical Analysis of Spectral Methods: Theory and Applications*, Society for Industrial and Applied Mathematics, Philadelphia, PA.
[51] Smith, R. C., 2013, *Uncertainty Quantification: Theory, Implementation, and Applications*, Vol. 12, Society for Industrial and Applied Mathematics, Philadelphia, PA.
[52] Feinberg, J., 2015, "Some Improvements and Applications of Non-Intrusive Polynomial Chaos Expansions," Ph.D. thesis, University of Oslo, Oslo, Norway.
[53] Feinberg, J., and Langtangen, H. P., 2015, "Chaospy: An Open Source Tool for Designing Methods of Uncertainty Quantification," J. Comput. Sci., **11**, pp. 46–57.
[54] Blatman, G., and Sudret, B., 2011, "Adaptive Sparse Polynomial Chaos Expansion Based on Least Angle Regression," J. Comput. Phys., **230**(6), pp. 2345–2367.
[55] Quicken, S., Donders, W. P., van Disseldorp, E. M., Gashi, K., Mees, B. M., van de Vosse, F. N., Lopata, R. G., Delhaas, T., and Huberts, W., 2016, "Application of an Adaptive Polynomial Chaos Expansion on Computationally Expensive Three-Dimensional Cardiovascular Models for Uncertainty Quantification and Sensitivity Analysis," ASME J. Biomech. Eng., **138**(12), p. 121010.